

VIP Very Important Paper

PTFE Enhances Discharge Performance of Carbon Cathodes in Potassium-Oxygen Batteries**

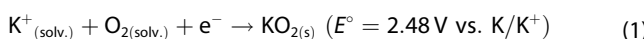
Jannis Küpper,^{*[a]} Simon Jakobi,^[a] and Ulrich Simon^[a]

Potassium-oxygen batteries (KOB) are a promising energy storage technology with high theoretical energy of 935 Wh/kg and long cycle life. Potential applications require the development of affordable cathode materials with high practical capacity. In this article, we show that low-cost polytetrafluoroethylene (PTFE) treatment increases the discharge performance of a commercial carbon paper cathode. Cross-sectional scanning electron microscopy reveals that PTFE alleviates mass transport limitations and facilitates homogeneous deposition of the discharge product potassium superoxide (KO_2) within the

cathode pore structure. Using electrochemical impedance spectroscopy, we found that PTFE, in combination with the appropriate electrolyte volume, can prevent pore flooding by the electrolyte. Free volume permits fast, gaseous oxygen transport throughout the cathode, which lowers mass transfer resistances and improves the rate capability. Moreover, PTFE enables high pore volume filling by KO_2 and, in turn, high discharge capacity. Our results demonstrate that controlling the mass transport is essential for high-performance cathodes for KOB.

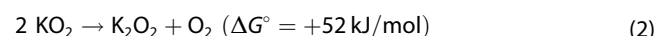
1. Introduction

The rapidly increasing demand for low-cost electrochemical energy storage has brought alkali metal-oxygen batteries (MOB) into the focus of immense research efforts. Especially the lithium-oxygen battery (LOB) was recognized early on as a potential technology to surpass the ubiquitous Li-ion battery (LIB), owing to its high theoretical specific energy of 3505 Wh/kg.^[1] However, practical capacities of LOB are still far behind desired and rechargeability is severely limited.^[2–3] The causes are found in the complex cell chemistry of LOB, which gives rise to numerous unintended side reactions. Recently, formation of highly reactive singlet oxygen (1O_2) during all stages of cycling was recognized as a major source of cell degradation.^[4] While not yet fully understood,^[5] there is strong evidence that 1O_2 generation is tied to the formation mechanism of the main discharge product lithium peroxide (Li_2O_2).^[6] By contrast, 1O_2 formation is not observed in KOB, where potassium superoxide (KO_2) is the main discharge product.^[5] The discharge reaction of KOB is a single electron transfer (SET) process [Eq. (1)].^[1]



The formation of KO_2 is thermodynamically and kinetically favored.^[7–8] A subsequent disproportionation reaction and

possible 1O_2 evolution, as observed in LOB, is energetically disfavored in KOB [Eq. (2)].^[7]



Formation of KO_2 as the discharge product has numerous additional benefits, which have been described in recent review articles.^[9–11] In brief, an outer-sphere SET enables fast kinetics of oxygen reduction reaction (ORR) and is highly reversible. Further, even simple carbon cathode materials show low cycling overpotential (≈ 50 mV), whereas LOB with precious metal catalysts typically exhibit substantial overpotential from 0.7 V to 1.5 V.^[1,12] The catalytic activity of graphitic carbon is indicated to outperform metal catalysts such as gold or platinum in KOB.^[7] KO_2 shows good long-term stability with low reactivity towards cell components, i.e., electrolyte and cathode materials.^[8] Operation of KOB in dry ambient air has been demonstrated, which could be an economical alternative to pure O_2 .^[13] Due to the worldwide abundance of K-containing minerals and without need for expensive precious metal catalysts, KOB could become a cost-effective energy storage technology.^[9]

Despite these features, KOB have not yet received considerable research attention. This may be ascribed to the lower formal specific energy of 935 Wh/kg compared to other MOB with multi-electron discharge reactions.^[10] In addition, limited cycle life is observed when a K metal anode is used. O_2 cross-over from the cathode compartment towards the K metal anode causes permanent self-discharge.^[14] When Ren et al. demonstrated the first KOB in 2014, cycle life was limited to ten cycles.^[1]

Several approaches have since been developed to curb self-discharge and K dendrite formation.^[14–20] Cong et al. reported an “organic” KOB cell design, in which $K-\beta''-Al_2O_3$ solid-state electrolyte (KBA) acts as an O_2 -impermeable separator.^[21] A liquid solution of potassium biphenyl complex (KBp) in 1,2-

[a] J. Küpper, S. Jakobi, Prof. U. Simon
Institute of Inorganic Chemistry
RWTH Aachen University
Landoltweg 1a, 52074 Aachen, Germany
E-mail: jannis.nicolas.kuepper@rwth-aachen.de

[**] PTFE: Polytetrafluoroethylene.

 Supporting information for this article is available on the WWW under <https://doi.org/10.1002/batt.202100095>

 © 2021 The Authors. *Batteries & Supercaps* published by Wiley-VCH GmbH. This is an open access article under the terms of the Creative Commons Attribution License, which permits use, distribution and reproduction in any medium, provided the original work is properly cited.

dimethoxyethane (DME) is used as anode active material, which offers low interfacial resistances with KBA. The standard cell potential is lowered compared to a K metal anode with $E_{(KB)/O_2} = 2.18$ V. Employing carbon paper as cathode, this configuration allows cycling at a limited areal discharge capacity (Q) of 0.25 mAh/cm 2 for 3000 cycles with an average current efficiency of 98.5 %.^[21]

For KOB to become an attractive technology, this remarkable rechargeability needs to be further developed towards significantly higher capacities. High-capacity LIB exhibit Q of 2.5 mAh/cm 2 to 4 mAh/cm 2 ,^[22] which may be considered as benchmark for rechargeable high-capacity energy storage. To enable high Q , it is critical to identify suitable cathode structures that account for the conversion-type cell chemistry of MOB. Both the cell chemistry of KOB and requirements for the ideal KOB cathode structure are largely unexplored.

When investigating novel cathode materials for MOB, electrolyte volume (V_{el}) is an easily overlooked parameter. However, V_{el} and the ratio of V_{el} to the combined mass of cathode and separator (V/m) were shown to be critical for the discharge performance of MOB.^[23–26] The discharge reaction [Eq. (1)] may only proceed in regions where the cathode surface is wetted by electrolyte. In addition, mass transport of K^+ and O_2 towards the cathode surface must be sufficient to sustain the demanded current rate.^[25,27] The rate of mass transfer is dictated by the distribution of solid electrode, liquid electrolyte and gaseous O_2 within the porous cathode, called the triple phase boundary (TPB).^[23,28] Ideally, the entire available cathode surface area is wetted by electrolyte and participates in the discharge reaction.^[23] Therefore, V/m must be sufficiently high to ensure complete wetting. However, too high V/m can drown the cathode by impeding O_2 transport towards the cathode surface area.^[24–25,29] The optimum V/m depends on a variety of parameters, for example, cathode porosity and wetting properties, and it can be identified by means of electrochemical impedance spectroscopy (EIS), which allows to measure the specific double-layer capacitance (C_{sp}) of an electrode in contact with electrolyte.^[23] C_{sp} , in turn, is directly proportional to the area of the solid-liquid interface.^[30]

A challenge of high-capacity MOB is the formation of insoluble reaction products, for example, KO_2 and Li_2O_2 , within the porous cathode structure. Q is inherently limited by the available pore volume, hence the pore volume should be utilized as efficiently as possible.^[31] However, relatively low degrees of pore volume utilization are typically achieved in MOB.^[32] Uneven discharge product growth can cause pore clogging and premature cell failure.^[33–34] The discharge product is expected to form preferably in regions with lowest mass transfer resistances, i.e., the boundaries of the cathode. As deposition proceeds in the boundaries, mass transport to the inner regions is hindered. It was found that discharge performance of LOB can be significantly improved by enabling transport of gaseous O_2 to the inner cathode regions,^[30] since the diffusion coefficient of gaseous O_2 in air ($D_{(O_2)air} \approx 10^{-2}$ cm 2 /s)^[31] is considerably higher than in electrolyte solvents, for example, dimethyl sulfoxide (DMSO) with $D_{(O_2)DMSO} \approx 10^{-6}$ cm 2 /s.^[35] A promising approach to optimize mass transfer is to change the

wetting properties of the gas diffusion layer (GDL).^[25,30–31] Hydrophobic treatment of the GDL was found to introduce repulsive interactions between cathode and electrolyte and to promote the formation of open channels for rapid gas transport.^[30]

In this work, we analyzed how PTFE modification of porous carbon cathodes affects the discharge performance of KOB. For this, we adopted the organic KOB design and studied the discharge processes for two commercial carbon paper GDL from Freudenberg as cathode, i.e., pristine H23 carbon paper compared to H23I2, a variant of H23 modified by 20 w.% PTFE via wet-impregnation. Both cathode materials are accessible for large scale applications. First, the optimum V/m was determined using EIS and battery testing. Then, the discharge performance of both materials was compared, and it was demonstrated that PTFE significantly enhances Q and rate capability. Cross-sectional scanning electron microscopy (SEM) and energy-dispersive X-ray spectroscopy (EDS) were used to examine the rate-dependent growth of KO_2 . PTFE was found to enable homogeneous KO_2 distribution and high degrees of pore filling, which leads to performance enhancement.

2. Results and Discussion

2.1. Effects of V/m and PTFE on Discharge Performance

To determine optimum V/m , a series of discharge tests with different V/m was conducted. Discharge testing was performed at a current density (J) of 0.5 mA/cm 2 , which is commonly used in KOB research. In addition, a low $J=0.1$ mA/cm 2 was tested to minimize mass transfer resistances and to identify a possible dependence of optimum V/m on the applied J .

Plots of Q vs. V/m for the tested J are displayed in Figure 1a for H23 as cathode and Figure 1b for H23I2 as cathode. The corresponding discharge profiles may be found in Figure S1 in the Supporting Information. In general, Q exhibits a strong dependence on V/m and higher Q was achieved for lower J at any given V/m . Both plots display a distinct maximum for Q , which is observed at $V/m=2.4$ μ L/mg for H23 and at $V/m=3.6$ μ L/mg for H23I2. The observed trends seem independent of the applied J . A notable exception is found for H23 with $V/m=2.0$ μ L/mg, where a discrepancy between low and high J is apparent. This observation may be explained by the J -dependence of KO_2 growth, which is further investigated in section 2.2.

The difference in optimum V/m between H23 and H23I2 is likely caused by PTFE-impregnation affecting the wetting of the cathode by electrolyte. Contact angle (Θ) measurements (Figure S2) for the polar electrolyte solvent DMSO (dielectric constant $\epsilon=47.2$)^[36] show good wetting of H23 and hydrophobicity of H23I2 ($\Theta_{H23I2}=110^\circ$). Thus, wetting of the pristine carbon fibers is energetically favored and H23 is readily soaked with electrolyte. On the other hand, PTFE treatment makes soaking of the cathode structure unfavorable, which should result in lower active surface area compared to H23. Nonetheless, H23I2 exhibits higher Q than H23 regardless of V/m , emphasizing that higher active surface area does not directly

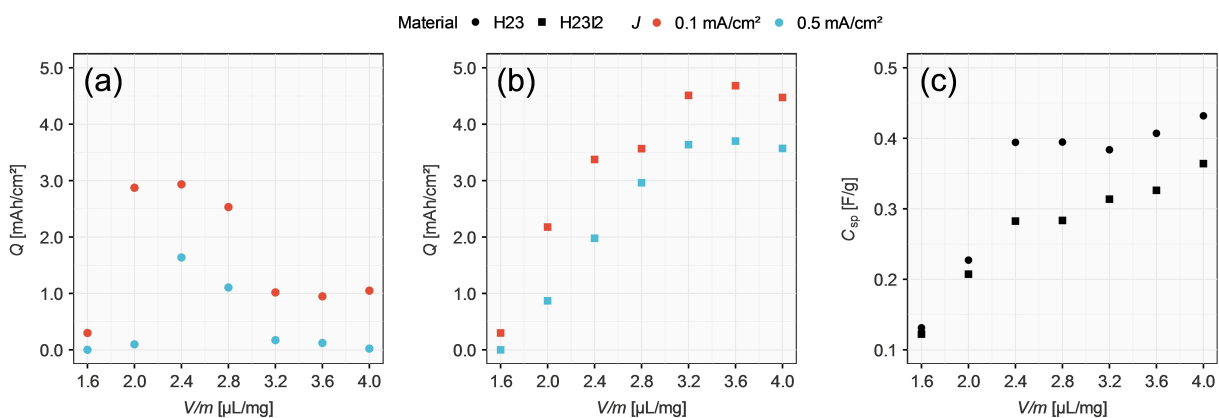


Figure 1. Plots of Q vs. V/m for a) H23 as cathode and for b) H23I2 as cathode at $J=0.1 \text{ mA/cm}^2$ (red) and $J=0.5 \text{ mA/cm}^2$ (blue). c) Plots of C_{sp} vs. V/m for H23 as cathode (circle) and H23I2 as cathode (square).

lead towards higher Q . Rather, V/m -dependent distribution of electrolyte within the cathode structure, i.e., the TPB, may be the Q -deciding factor, which agrees with findings for LOB.^[25,29–30]

C_{sp} was determined for V/m ranging from $1.6 \mu\text{L}/\text{mg}$ to $4.0 \mu\text{L}/\text{mg}$ from EIS spectra (Figure S3) via a previously reported approach.^[37] The obtained plots of C_{sp} vs. V/m are shown in Figure 1c. For H23, C_{sp} increases from $V/m=1.6 \mu\text{L}/\text{mg}$ ($C_{sp} \approx 0.1 \text{ F/g}$) to $V/m=2.4 \mu\text{L}/\text{mg}$ ($C_{sp} \approx 0.4 \text{ F/g}$), where a saddle point is reached, which indicates that the cathode may only be partially wetted below $V/m=2.4 \mu\text{L}/\text{mg}$. Further addition of electrolyte up to V/m of $3.2 \mu\text{L}/\text{mg}$ does not affect C_{sp} significantly. For $V/m=3.6 \mu\text{L}/\text{mg}$ and above the cathode was observed to be submerged in electrolyte and the additional C_{sp} increase is likely caused by wetting of the current collector. Taking the discharge performance (Figure 1a) into account, a V/m higher than $2.4 \mu\text{L}/\text{mg}$ is detrimental to Q . Once the entire cathode surface area is wetted, higher V/m increases the thickness of the electrolyte layer. O_2 transport is increasingly hindered by the longer diffusion pathway to the cathode surface. For H23, the highest Q is achieved for the minimum V_{el} where C_{sp} reaches the maximum.

The development of C_{sp} for H23I2 differs significantly from H23. While C_{sp} is similar for $V/m=1.6 \mu\text{L}/\text{mg}$ and $V/m=2.0 \mu\text{L}/\text{mg}$, it is lower at $V/m=2.4 \mu\text{L}/\text{mg}$ ($C_{sp} \approx 0.3 \text{ F/g}$) than for H23 ($C_{sp} \approx 0.4 \text{ F/g}$). Moreover, the C_{sp} keeps increasing with higher V/m up to $4.0 \mu\text{L}/\text{mg}$, suggesting that the cathode surface is progressively wetted. Highest Q is achieved with $V/m=3.6 \mu\text{L}/\text{mg}$, which is not reflected in a maximum or saddle point of C_{sp} . At $V/m=4.0 \mu\text{L}/\text{mg}$, C_{sp} is further increased, suggesting that the pore volume of the cathode is not fully filled by electrolyte at $V/m=3.6 \mu\text{L}/\text{mg}$. This may explain the performance-increasing effect of PTFE: Hydrophobic treatment can prevent complete pore flooding, allowing for gaseous O_2 towards the inner regions.

Since O_2 transport in gas phase is faster than diffusion through the liquid electrolyte, PTFE may also improve the rate capability.^[25] Discharge testing was performed with the respective optimum V/m for both materials at three J of 0.1 mA/cm^2 , 0.5 mA/cm^2 and 1.0 mA/cm^2 .

In Figure 2 the discharge profiles for H23 (a) and H23I2 (b) are shown. One voltage plateau is visible for both materials at all tested J and a second voltage plateau, which could indicate formation of K_2O_2 , is not observed.^[21] The sharp drop in potential near cell failure is commonly observed for MOB and is generally tied to the growth of discharge products within the cathode.^[38–39] In general, the discharge overpotential (η_{dis}) significantly increases with higher J while Q decreases. Comparing the cathode materials, η_{dis} is significantly lower for H23I2 than H23 at all tested J . A reduction of η_{dis} by 0.02 V is observed for $J=0.1 \text{ mA/cm}^2$ and up to 0.2 V for $J=1.0 \text{ mA/cm}^2$. Moreover, Q of 2.9 mAh/cm^2 was obtained for H23 and 4.7 mAh/cm^2 for H23I2, which represents a 62% increase in Q enabled by PTFE treatment. This beneficial effect is more pronounced for higher J , with up to 300% increase in Q for $J=1.0 \text{ mA/cm}^2$. These findings demonstrate that PTFE treatment, in combination with the optimum V/m , can markedly enhance the discharge performance of carbon cathodes.

2.2. Effects of PTFE Treatment on KO_2 Growth and Cell Failure

To elucidate underlying processes enabling the performance improvement by PTFE treatment, a study of cathode microstructure, and formation of KO_2 within, is needed. The GDL tested in this work possess a thickness $> 200 \mu\text{m}$. Inhomogeneous KO_2 growth along the thickness is expected.^[40] Analysis of cathode cross sections is therefore required to accurately survey KO_2 formation. Cross-sectional SEM images of H23 cathodes are shown in Figure 3. SEM image (a) displays the cross section of pristine H23. Cells were discharged at different J : 0.1 mA/cm^2 (b–d), 0.5 mA/cm^2 (e) and 1.0 mA/cm^2 (f). The solid discharge product, which was identified as KO_2 by means of X-ray diffraction and Raman spectroscopy (Figure S4), is visible as bright deposits within the porous carbon paper structure. Spatial histograms of the KO_2 distribution along the cross sections, which were obtained from EDS K maps (see Figure S5), are overlaid on the right side of the SEM images. It is noted that the histograms reflect the relative spatial distribution of KO_2 , while the intensity is not directly indicative

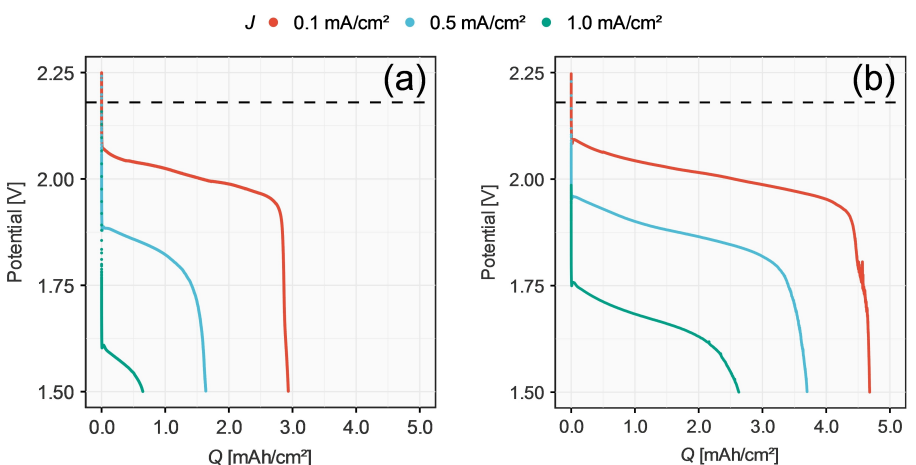


Figure 2. Discharge profiles for KOB cells with a) H23 as cathode and b) H23I2 as cathode for $J=0.1 \text{ mA/cm}^2$ (red), $J=0.5 \text{ mA/cm}^2$ (blue), and $J=1.0 \text{ mA/cm}^2$ (green). The dashed black line indicates the open circuit potential $E^\circ(\text{KBP}/\text{O}_2)=2.18 \text{ V}$.

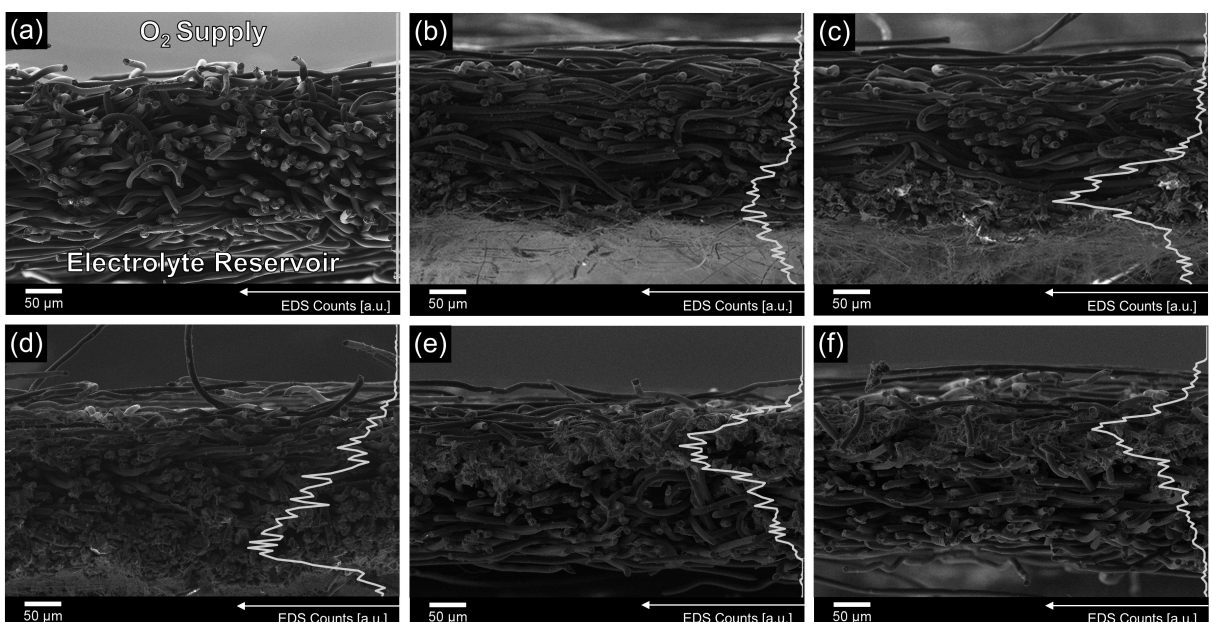


Figure 3. Cross-sectional SEM images of H23 cathodes for different J and DoD. Spatial histograms of KO_2 distribution (white line plots) are overlaid on the right side of the SEM images. a) Pristine H23. b) $J=0.1 \text{ mA/cm}^2$, 22% DoD. c) $J=0.1 \text{ mA/cm}^2$, 66% DoD. d) $J=0.1 \text{ mA/cm}^2$, 100% DoD. e) $J=0.5 \text{ mA/cm}^2$, 100% DoD. f) $J=1.0 \text{ mA/cm}^2$, 100% DoD.

of the absolute quantity of KO_2 .^[41] Additional SEM images may be found in Figure S6 to further illustrate the spatial distribution of KO_2 and its morphology.

Limited-capacity discharge was performed at $J=0.1 \text{ mA}/\text{cm}^2$ to two Q , which correspond to depths of discharge (DoD) of 22% and 66%, respectively. At low DoD of 22% (Figure 3b), KO_2 mainly forms in regions close to the electrolyte reservoir, where K^+ transport is likely to be fast and O_2 transport to be slow. Residues of glass fiber paper from the electrolyte reservoir are visibly attached to the cathode, indicating that growth is initiated at the cathode-electrolyte reservoir interface. With increasing DoD (Figure 3c) the available pore volume in this region is gradually occupied by KO_2 . Therefore, KO_2 growth for low J is seemingly preferred in regions with high K^+ transport.

After complete discharge (Figure 3d), a significant fraction of pore volume is filled with KO_2 . Once the regions close to the electrolyte reservoir are occupied by KO_2 , its growth is seemingly shifted towards inner cathode regions. However, full discharge does not lead to high degrees of filling of the cathode structure. Open pore space and free cathode surface are available in areas near the O_2 supply. Cell failure is therefore not likely to be caused by limited O_2 transport or lack of accessible surface area. One aspect, that is negatively affected by dense KO_2 at the cathode-reservoir interface, is K^+ transport towards the regions where KO_2 growth is favored. Electrolyte displacement by KO_2 may effectively decrease the ionic conductivity of the electrolyte,^[25] leading to high K^+ mass transfer resistance and cell failure.

At higher J (Figure 3e–f), the spatial histograms indicate that KO_2 is formed primarily in regions close to the O_2 supply, i.e., with high O_2 availability. Lower amounts of KO_2 are formed near the electrolyte reservoir. These inner sections of cathode are expected to be fully wetted by electrolyte and cathode surface area to be accessible. Thus, cell failure appears to be caused by O_2 transport limitations, which is in accordance with other studies.^[25] As cathode pores close to the O_2 supply become clogged by KO_2 , O_2 transport to the inner regions is diminished. This could result in low degrees of pore volume utilization and is reflected in low Q for higher $J=0.5 \text{ mA/cm}^2$ ($Q \approx 1 \text{ mAh/cm}^2$) and $J=1 \text{ mA/cm}^2$ ($Q \approx 0.1 \text{ mAh/cm}^2$).

The previously noted discrepancy in Q for $V/m=2.0 \mu\text{L}/\text{mg}$ (Figure 1a) can be explained by the observed J -dependence of KO_2 formation. For $V/m=2.0 \mu\text{L}/\text{mg}$, the cathode is underfilled and primarily wetted in regions close to the electrolyte reservoir, as the electrolyte is added directly to the reservoir during assembly. SEM images (Figure 3b–d) show that these areas are most active for low J and regions near the O_2 supply do not exhibit significant KO_2 deposition. Therefore, high Q may be obtained at slow rates with V/m of $2.0 \mu\text{L}/\text{mg}$ despite the apparent underfilling, because additional V_{el} would lead to wetting of regions that are electrochemically inactive.

Regardless of applied J , H23 seemingly does not facilitate homogeneous growth of KO_2 , which is required for large degrees of pore filling and high Q . Analogous to H23, investigations of KO_2 growth were performed with H23I2 as cathode. Cross-sectional SEM images for a variation of J are displayed in Figure 4. Additional SEM images, which show the discharge product distribution and its morphology, may be found in Figure S7.

Pristine H23I2 is shown in Figure 4a. Discharge at $J=0.1 \text{ mA/cm}^2$ was performed to limited Q corresponding to 14% DoD (Figure 4b) and 41% DoD (Figure 4c). At these low DoD, KO_2 deposits are visible throughout the entire cathode structure. In addition, the respective spatial histograms (see Figure S8 for EDS K maps) indicate that KO_2 growth is not concentrated at the cathode-reservoir interface for low J , as it is observed for H23 (Figure 3b–c). For complete discharge (Figure 4d), the available pore volume is largely filled by KO_2 and the cathode surface is barely visible. The rather uniform deposition of KO_2 suggests that for low J Q may not be limited by mass transport. Rather, the deposition of electronically insulating KO_2 ^[42] progressively passivates the surface of the cathode carbon fibers. The active surface area decreases until charge transfer is effectively prevented.^[40] In addition, near-complete filling by KO_2 may also cause electrolyte displacement from the cathode structure. While a high degree of pore volume utilization is desirable for high energy density, lack of electrolyte inside the cathode could be detrimental to charge processes. We are currently investigating the effects of PTFE treatment on the rechargeability and cycle life of KOB.

For higher $J=0.5 \text{ mA/cm}^2$ (Figure 4e) and $J=1.0 \text{ mA/cm}^2$ (Figure 4f), PTFE treatment also enables KO_2 growth throughout the cathode structure. This contrasts with H23, where KO_2 deposits are concentrated in O_2 -rich regions (Figure 3e–f). Nevertheless, lower Q and less efficient pore filling are observed at these higher rates compared to $J=0.1 \text{ mA/cm}^2$. While the KO_2 growth is rather homogeneous, large KO_2 deposits appear to induce mass transfer limitations at high DoD.

These findings suggest that PTFE treatment improves the rate capability through faster O_2 transport throughout the

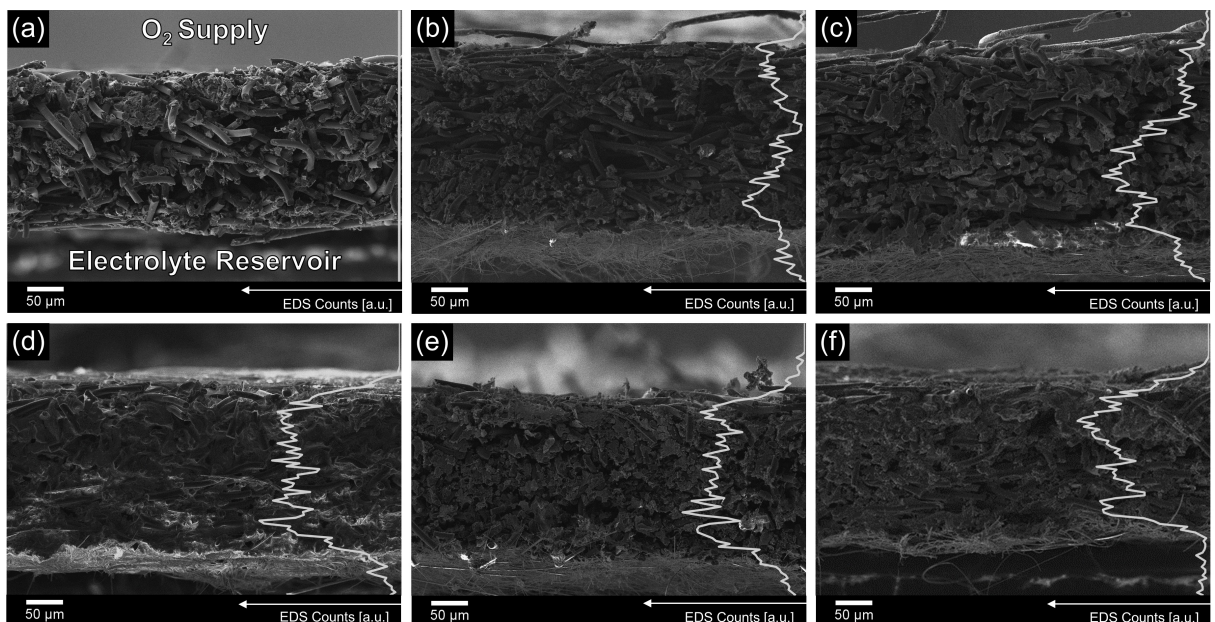


Figure 4. Cross-sectional SEM images of H23I2 cathodes for different J and DoD. Spatial histograms of KO_2 distribution (white line plots) are overlaid on the right side of the SEM images. a) Pristine H23I2. b) $J=0.1 \text{ mA/cm}^2$, 14% DoD. c) $J=0.1 \text{ mA/cm}^2$, 41% DoD. d) $J=0.1 \text{ mA/cm}^2$, 100% DoD. e) $J=0.5 \text{ mA/cm}^2$, 100% DoD. f) $J=1.0 \text{ mA/cm}^2$, 100% DoD.

cathode and increases Q by enabling more homogeneous KO_2 growth.

3. Conclusion

In this article, the effects of PTFE treatment on the discharge performance of a commercial carbon paper cathode are investigated. Hydrophobic properties of PTFE are observed to prevent pore flooding, which enables transport of gaseous oxygen throughout the cathode pore structure. By enhancing oxygen transport, PTFE is found to effectively raise the rate capability. Furthermore, PTFE is observed to facilitate homogeneous KO_2 deposition, enabling high degrees of pore filling and high discharge capacity. In our case, the discharge capacity appears to only be limited by the available pore volume for slow rates. To achieve high energy density KOB, future studies should therefore aim to increase both cathode porosity and mass transport. Promising approaches to further increase mass transport, which we are currently investigating, are tuning of oxygen solubility^[43] and superoxide solvation^[44] of the electrolyte, as well as changing the oxygen pressure.^[40,43] In summary, our results demonstrate that PTFE treatment improves mass transport and enhances the discharge performance of carbon cathodes in KOB.

Experimental Section

Chemicals and Materials

Dimethyl sulfoxide (DMSO, 99.9%, anhydrous, Sigma-Aldrich) and 1,2-dimethoxyethane (DME, 99.5%, anhydrous, Sigma-Aldrich) were stored over activated 3 Å molecular sieve at least 14 days before use. Moisture contents were determined by Karl-Fischer-Titration (KFT) to be <20 ppm. Biphenyl (Bp, 99%, Sigma-Aldrich) was vacuum-dried at RT for 3 days and transferred to an argon-filled glovebox ($H_2O < 0.1$ ppm, $O_2 < 0.1$ ppm) without air exposure. KPF_6 (99.5%, Sigma-Aldrich) was vacuum-dried at 110 °C for 8 h and transferred to the glovebox without air exposure. $K-\beta''$ -alumina disks (KBA, diameter $\varnothing = 20$ mm, thickness $T = 1.0$ mm, Ionotec, UK) and K metal (99.95%, Sigma-Aldrich) were used as received. Circular disks were punched of H23 ($m = 14.6 \text{ mg} \pm 0.1 \text{ mg}$, $\varnothing = 14$ mm, $T = 0.211$ mm, Freudenberg, Germany), H23I2 ($m = 17.6 \text{ mg} \pm 0.1 \text{ mg}$, $\varnothing = 14$ mm, $T = 0.222$ mm, 20 w.-% PTFE, Freudenberg, Germany), Grade GF/A ($m = 10.2 \text{ mg} \pm 0.1 \text{ mg}$, $\varnothing = 16$ mm, Whatman, UK) and Grade GF/B ($m = 22.0 \text{ mg} \pm 0.1 \text{ mg}$, $\varnothing = 14$ mm, Whatman, UK) glass fiber filter and Cu foam ($\varnothing = 16$ mm, $T = 2.0$ mm, > 99%, Alfa Aesar, USA), then dried at 105 °C overnight and immediately transferred to the glovebox.

Battery Cell Assembly

Battery cells were based on ECC-Air cells (EL-Cell, Germany). A modular cell inlay was built in-house to adapt the ECC-Std cell to the organic $K-O_2$ battery design^[21] (see Figure S9 and Figure S10). Inlay components were dried at 105 °C overnight and transferred to the glovebox while hot. Cell assembly was performed in the glovebox. Cu foam and grade GF/B filter were inserted into the anode compartment of the inlay. Then, 200 μL of 3.0 M KBp in DME were added. KBA disk was placed on top. The upper polyether

ether ketone (PEEK) inlay component was put into place and the anode compartment was sealed with PEEK clamps. Grade GF/A was inserted into the cathode compartment. A varying volume of 0.5 M KPF_6 in DMSO electrolyte ($H_2O < 3$ ppm) was added. A H23 or H23I2 disk was inserted, and a perforated stainless-steel current collector disk ($\varnothing = 16$ mm, $T = 1$ mm) was placed on top. A copper spring was added for compression. The inlay was transferred to the ECC-Std cell housing and the cell was sealed with the cell clamp.

Electrochemical Measurements

Cells were removed from the glovebox and connected to the O_2 supply ($p = 2.0$ atm, 99.999%, $H_2O < 3$ ppm, Westfalen AG, Germany). Cells were flushed under rapid O_2 flow for 2 min. Battery tests were performed with CTS battery tester (Basytec, Germany). A 75 min resting step at open-circuit potential was performed prior to battery testing. Discharge currents were normalized to the nominal surface area of cathode materials ($A = 1.54 \text{ cm}^2$). The cutoff cell voltage was 1.50 V. Electrochemical impedance spectroscopy (EIS) was performed with a Vertex. One potentiostat (Ivium, Netherlands) with battery cells in the glovebox. EIS spectra were recorded at open-circuit voltage in the frequency range of 100 kHz to 0.32 Hz with 9 points per decade and 5 mV excitation amplitude. Spectrum quality was tested with LIN-KK tool (Karlsruhe Institute of Technology, Germany) and data with relative residuals below 2% was used for equivalent circuit model fitting.

Analysis Methods

Samples were prepared by removing cathodes from cells in the glovebox and rinsing thoroughly with DME. Scanning electron microscopy (SEM) was performed at an acceleration voltage of 10 kV with a LEO Supra35VP (Carl Zeiss AG, Germany) SEM device with integrated energy-dispersive x-ray spectroscopy (EDS) INCA Energy 200 detector (Oxford Instruments, UK). Cross-sections of cathodes were obtained by cutting the cathode using a scalpel. Samples were transferred to the SEM device under argon counterflow. Spatial histograms were produced by data processing of $K K_{\alpha}$ -line mappings, obtained from EDS, into 96 vertically aligned line scans. Integrating the signal counts of the line scans yielded histograms with spatial resolution of 4.4 μm . Raman spectroscopy was performed in argon atmosphere with a LamRAM 300 spectrometer ($\lambda = 633$ nm, $P = 12$ mW, Horiba, Japan). X-ray powder diffraction was carried out in argon atmosphere using a STOE StadiP powder diffractometer (Stoe&Cie, Germany).

Acknowledgements

This research was funded by the Deutsche Forschungsgemeinschaft (DFG, German Research Foundation) – GRK 1856. The authors thank the team of the mechanical workshop of the Institute of Inorganic Chemistry at RWTH Aachen University for the support in design and construction of the battery cells and T. Storp for the support in XRD measurements. Open Access funding enabled and organized by Projekt DEAL.

Conflict of Interest

The authors declare no conflict of interest.

Keywords: cathode design · discharge capacity · impedance spectroscopy · KO₂ growth · potassium-oxygen batteries

- [1] X. Ren, Y. Wu, *J. Am. Chem. Soc.* **2013**, *135*, 2923–2926.
- [2] M. Balaish, J. W. Jung, I. D. Kim, Y. Ein-Eli, *Adv. Funct. Mater.* **2020**, *30*, 1808303.
- [3] P. Wunderlich, J. Küpper, U. Simon, *Materials* **2020**, *13*, 43.
- [4] N. Mahne, B. Schafzahl, C. Leypold, M. Leypold, S. Grumm, A. Leitgeb, G. A. Strohmeier, M. Wilkening, O. Fontaine, D. Kramer, C. Slugovc, S. M. Borisov, S. A. Freunberger, *Nat. Energy* **2017**, *2*, 1–9.
- [5] G. Houchins, V. Pande, V. Viswanathan, *ACS Energy Lett.* **2020**, *5*, 1893–1899.
- [6] E. Mourad, Y. K. Petit, R. Spezia, A. Samojlov, F. F. Summa, C. Prehal, C. Leypold, N. Mahne, C. Slugovc, O. Fontaine, S. Brutti, S. A. Freunberger, *Energy Environ. Sci.* **2019**, *12*, 2559–2568.
- [7] P. H. Reinsberg, A. Koellisch, H. Baltruschat, *Electrochim. Acta* **2019**, *313*, 223–234.
- [8] N. Xiao, R. T. Rooney, A. A. Gewirth, Y. Wu, *Angew. Chem. Int. Ed.* **2018**, *57*, 1227–1231; *Angew. Chem.* **2018**, *130*, 1241–1245.
- [9] L. Qin, L. Schkeryantz, J. Zheng, N. Xiao, Y. Wu, *J. Am. Chem. Soc.* **2020**, *142*, 11629–11640.
- [10] N. Xiao, X. Ren, W. D. McCulloch, G. Gourdin, Y. Wu, *Acc. Chem. Res.* **2018**, *51*, 2335–2343.
- [11] J. Park, J. Y. Hwang, W. J. Kwak, *J. Phys. Chem. Lett.* **2020**, *11*, 7849–7856.
- [12] K. Chen, D.-Y. Yang, G. Huang, X.-B. Zhang, *Acc. Chem. Res.* **2021**, *54*, 632–641.
- [13] L. Qin, N. Xiao, S. Zhang, X. Chen, Y. Wu, *Angew. Chem. Int. Ed.* **2020**, *59*, 10498–10501; *Angew. Chem.* **2020**, *132*, 10584–10587.
- [14] X. Ren, K. C. Lau, M. Yu, X. Bi, E. Kreidler, L. A. Curtiss, Y. Wu, *ACS Appl. Mater. Interfaces* **2014**, *6*, 19299–19307.
- [15] W. Yu, K. C. Lau, Y. Lei, R. Liu, L. Qin, W. Yang, B. Li, L. A. Curtiss, D. Zhai, F. Kang, *ACS Appl. Mater. Interfaces* **2017**, *9*, 31871–31878.
- [16] W. D. McCulloch, X. Ren, M. Yu, Z. Huang, Y. Wu, *ACS Appl. Mater. Interfaces* **2015**, *7*, 26158–26166.
- [17] A. Eftekhar, Z. Jian, X. Ji, *ACS Appl. Mater. Interfaces* **2017**, *9*, 4404–4419.
- [18] X. D. Ren, M. F. He, N. Xiao, W. D. McCulloch, Y. Y. Wu, *Adv. Energy Mater.* **2017**, *7*.
- [19] N. Xiao, G. Gourdin, Y. Wu, *Angew. Chem. Int. Ed.* **2018**, *57*, 10864–10867; *Angew. Chem.* **2018**, *130*, 11030–11033.
- [20] P. Gilmore, V. B. Sundaresan, *Batteries & Supercaps* **2019**, *2*, 662–662; *Supercaps* **2019**, *2*, 662–662.
- [21] G. Cong, W. Wang, N. C. Lai, Z. Liang, Y. C. Lu, *Nat. Mater.* **2019**, *18*, 390–396.
- [22] J. T. Lee, C. Jo, M. De Volder, *Proc. Natl. Acad. Sci. USA* **2020**, *117*, 21155–21161.
- [23] G. Gourdin, N. Xiao, W. McCulloch, Y. Wu, *ACS Appl. Mater. Interfaces* **2019**, *11*, 2925–2934.
- [24] C. Xia, C. L. Bender, B. Bergner, K. Peppler, J. Janek, *Electrochem. Commun.* **2013**, *26*, 93–96.
- [25] F. Wang, X. Li, *ACS Appl. Mater. Interfaces* **2018**, *10*, 26222–26232.
- [26] P. Wunderlich, J. Küpper, U. Simon, *Batteries* **2020**, *6*, 36.
- [27] J. Read, K. Mutolo, M. Ervin, W. Behl, J. Wolfenstine, A. Driedger, D. Foster, *J. Electrochem. Soc.* **2003**, *150*, A1351.
- [28] C. Tran, X.-Q. Yang, D. Qu, *J. Power Sources* **2010**, *195*, 2057–2063.
- [29] S. S. Zhang, D. Foster, J. Read, *J. Power Sources* **2010**, *195*, 1235–1240.
- [30] F. Wang, X. Li, *ACS Omega* **2018**, *3*, 6006–6012.
- [31] F. Wang, X. Li, X. Hao, J. Tan, *ACS Appl. Mater. Interfaces* **2020**, *3*, 2258–2270.
- [32] P. Albertus, G. Girishkumar, B. McCloskey, R. S. Sánchez-Carrera, B. Kozinsky, J. Christensen, A. C. Luntz, *J. Electrochem. Soc.* **2011**, *158*, A343.
- [33] I. Bardenhagen, M. Fenske, D. Fenske, A. Wittstock, M. Bäumer, *J. Power Sources* **2015**, *299*, 162–169.
- [34] I. Bardenhagen, O. Yezerska, M. Augustin, D. Fenske, A. Wittstock, M. Bäumer, *J. Power Sources* **2015**, *278*, 255–264.
- [35] P. P. Bawol, P. H. Reinsberg, H. Baltruschat, *Anal. Chem.* **2018**, *90*, 14145–14149.
- [36] C. J. Bondue, P. P. Bawol, A. A. Abd-El-Latif, P. Reinsberg, H. Baltruschat, *J. Phys. Chem. C* **2017**, *121*, 8864–8872.
- [37] K. B. Knudsen, J. E. Nichols, T. Vegge, A. C. Luntz, B. D. McCloskey, J. Hjelm, *J. Phys. Chem. C* **2016**, *120*, 10799–10805.
- [38] J. E. Nichols, B. D. McCloskey, *J. Phys. Chem. C* **2017**, *121*, 85–96.
- [39] V. Viswanathan, K. S. Thygesen, J. S. Hummelshøj, J. K. Nørskov, G. Girishkumar, B. D. McCloskey, A. C. Luntz, *J. Chem. Phys.* **2011**, *135*, 214704.
- [40] N. Xiao, X. Ren, M. He, W. D. McCulloch, Y. Wu, *ACS Appl. Mater. Interfaces* **2017**, *9*, 4301–4308.
- [41] D. E. Newbury, N. W. Ritchie, *Scanning* **2013**, *35*, 141–168.
- [42] O. Gerbig, R. Merkle, J. Maier, *Adv. Funct. Mater.* **2015**, *25*, 2552–2563.
- [43] P. H. Reinsberg, A. Koellisch, P. P. Bawol, H. Baltruschat, *Phys. Chem. Chem. Phys.* **2019**, *21*, 4286–4294.
- [44] N. Aetukuri, G. O. Jones, L. E. Thompson, C. Ozgit-Akgun, E. Akca, G. Demirci, H. C. Kim, D. S. Bethune, K. Virwani, G. M. Wallraff, *ACS Energy Lett.* **2018**, *3*, 2342–2348.

Manuscript received: April 29, 2021

Revised manuscript received: June 18, 2021

Accepted manuscript online: June 18, 2021

Version of record online: July 5, 2021